RSC Advances

PAPER

View Article Online
View Journal | View Issue

Cite this: *RSC Adv.*, 2026, **16**, 4228

Improved electrical and bioactivities of lead-free BNT–SBT ceramics by STZ additive and post-sintering processes

Kamonporn Saenkam,[a] Waraporn Boontakam,[a] Phanrawee Sriprapha,[a] Pichitchai Butnoi,[b] Kamonpan Pengpat,[a] Chamnan Randorn[ce] and Gobwute Rujijanagul *[ade]

This study examined the effects of $Sr(Ti_{0.85}Zr_{0.15})O_3$ (STZ) additive and post-sintering treatments on the electrical and biological properties of lead-free $(1-x)[0.7(Bi_{0.5}Na_{0.5})TiO_3–0.3(Sr_{0.7}Bi_{0.2})TiO_3]–xSr(Ti_{0.85}Zr_{0.15})O_3$ or $((1-x)(BNT–SBT)–xSTZ)$ ceramics synthesized by solid-state reaction. All compositions showed coexistence of rhombohedral and tetragonal phases, with increased STZ promoting the rhombohedral phase. The $x = 0.15$ composition exhibited favorable results, featuring a broad temperature coefficient of capacitance (TCC) stability range (±15% from 38–310 °C), a 43% increase in energy storage density, 92.90% energy efficiency, strong breakdown strength (95 kV cm^{-1}), and excellent thermal stability, with only 1.48% energy density variation between 25 and 125 °C. Its initial electrostrain of 0.06% was notably low. Post-sintering aging enhanced electrostrain to 0.33% representing a 450% increase and significantly improving electromechanical response. Cytotoxicity testing confirmed excellent cell viability, and bioactivity in simulated body fluid, initially moderate, was notably enhanced by β-tricalcium phosphate surface coating. These results highlight the biomedical potential of the optimized $x = 0.15$ ceramic composition.

Received 1st October 2025
Accepted 23rd December 2025

DOI: 10.1039/d5ra07450a

rsc.li/rsc-advances

1. Introduction

Due to increasing environmental concerns over the toxicity and volatility of lead oxide found in many lead-based piezoelectric ceramics, recent research has shifted toward the development of lead-free alternatives. Materials such as $BaTiO_3$ (BT), $(Bi_{0.5}K_{0.5})TiO_3$ (BKT), $K_{0.5}Na_{0.5}NbO_3$ (KNN), and $Bi_{0.5}Na_{0.5}TiO_3$ (BNT) have gained considerable attention for their promising electrical properties.[1–3] Among these, BNT-based ceramics stand out for their excellent ferroelectric behavior,[4,5] typically exhibiting high maximum polarization (~43 μC cm^{-2}), attributed to the hybridization between Bi 6s and O 2p orbitals.[2,6,7] However, BNT ceramics also suffer from a large coercive field (~73 kV cm^{-1})[2,6,7] and high electrical conductivity, which hinder effective polarization during the poling process and limit their practical applications.[8,9] To improve the properties of BNT, various modifications and complex solid solutions have been explored. Furthermore, modified BNT-based systems such as BNT–BKT (BNKT),[1–3] BNT–$Ba(Al_{0.5}Sb_{0.5})O_3$,[10] BNT–BKT–$SrTiO_3$,[11] BNT–BT–KNN,[12] BNT–BKT–$Ba(Fe_{0.5}Nb_{0.5})O_3$,[13] and BNT–BT–$(Sr_{0.7}Bi_{0.2})TiO_3$ [14] and BNKT–$Ba(Nb_{0.01}Ti_{0.99})O_3$–$BiFeO_3$ [15] have demonstrated excellent strain behavior, making them strong candidates for electromechanical applications.[1,2]

For energy storage applications, the induced relaxor state in BNT-based materials has been shown to significantly improve their performance.[3,16] Therefore, various composition design strategies have been employed by incorporating materials such as $NaTaO_3$,[17] $BiTi_{0.5}Zn_{0.5}O_3$,[18] $Bi(Zn_{2/3}Nb_{1/3})O_3$,[19] $Sr_{0.7}Bi_{0.2}TiO_3$,[20] $NaNbO_3$,[21] and $AgNbO_3$,[22] and $Sr(Ti_{0.85}Zr_{0.15})O_3$.[23] Additionally, BNT–$(Sr_{0.7}Bi_{0.2})TiO_3$ (or BNT–SBT) based ceramics also exhibit high remanent polarization.[24] Furthermore, recent studies suggest the BNT–SBT based ceramics also offer a promising energy storage density.[4,20,25] Therefore, modifying BNT–SBT ceramics with other materials may further enhance their overall properties.

Recently, $Sr(Zr_xTi_{1-x})O_3$ ceramics have attracted considerable research interest due to their notable dielectric properties.[26] This ceramic system is developed by substituting Ti^{4+} with Zr^{4+} at the B-site of the ABO_3 perovskite structure.[27–29] The larger ionic radius of Zr^{4+} induces lattice distortion, which enhances the dielectric characteristics of the ceramic. Moreover, partial substitution of Zr^{4+} (up to 5 mol%) significantly

[a]*Department of Physics and Materials Science, Faculty of Science, Chiang Mai University, Chiang Mai 50200, Thailand. E-mail: gobwute.ruji@cmu.ac.th*
[b]*Department of Metallurgical Technology, Faculty of Technical Education, Rajamangala University of Technology Krungthep, Bangkok 10120, Thailand*
[c]*Department of Chemistry, Faculty of Science, Chiang Mai University, Chiang Mai, 50200, Thailand*
[d]*Science and Technology Research Institute, Chiang Mai University, Chiang Mai 50200, Thailand*
[e]*Materials Science Research Center, Faculty of Science, Chiang Mai University, Chiang Mai 50200, Thailand*

improves dielectric breakdown strength (up to 14.4 kV cm^{-1}), making these ceramics a promising candidate for high-voltage capacitor applications.[27] Specifically, the composition of STZ has been employed as a modifier in BNT-based ceramics to reduce remanent polarization (P_r) and enhance breakdown strength. These modifications contribute to improved energy storage density, higher efficiency, and overall enhancement of dielectric performance.[23]

Since BNT–SBT ceramics exhibit promising electrical properties, and the incorporation of STZ has been shown to enhance the performance of BNT-based ceramics, it is worthwhile to investigate the BNT–SBT system modified with STZ. In this study, BNT–SBT–STZ ceramics were fabricated, and their properties were investigated, including phase formation, microstructure, dielectric behavior, energy density properties, and electrostrain performance. However, it is important to note that while promoting a relaxor state can effectively enhance certain electrical properties, such as energy storage density, a higher degree of relaxor behavior often leads to a reduction in electrostrain performance. To overcome this trade-off, many post-sintering treatments have been proposed to optimize the material properties.[1,2] Therefore, in this study, the samples were subjected to an aging treatment after sintering. Additionally, with the growing interest in piezoelectric materials for medical applications,[30,31] several lead-free piezoceramics have been developed to explore their potential for use in the human body, offering both biocompatibility and favorable electrical properties.[30–34] Therefore, the biological properties of the fabricated ceramics were also evaluated in this study. To enhance their bioactivity, the ceramics were coated with a bioactive material, and their bioactive performance was subsequently evaluated.

2. Experimental procedure

The $(1 - x)[0.7(Bi_{0.5}Na_{0.5})TiO_3–0.3(Sr_{0.7}Bi_{0.2})TiO_3]–xSr(Ti_{0.85}Zr_{0.15})O_3$ or $((1 - x)$[BNT–SBT]–xSTZ) ceramics with $x = 0$, 0.05, 0.10, 0.15, and 0.20 were synthesized *via* the conventional solid-state route. The high-purity reagent-grade powders used in this work were BiO_3 (99.9%, average particle size 10 μm, Sigma-Aldrich), $NaCO_3$ (99.5%, average particle size 9 μm, Sigma-Aldrich), TiO_2 (99%, average particle size 2–3 μm, Sigma-Aldrich), $SrCO_3$ (98%, average particle size 2 μm, Sigma-Aldrich), and ZrO_2 (99%, average particle size 5 μm, Sigma-Aldrich). The raw powders were dried at 120 °C for 24 h to remove moisture. The powders were then weighed according to the stoichiometric formula of $(1 - x)$[BNT–SBT]–xSTZ, ball-milled in 99.9% ethanol for 24 h, dried, and subsequently calcined at 850 °C for 3 h in air. After adding 4 wt% polyvinyl alcohol (PVA) as a binder, the powders were uniaxially pressed into 10 mm pellets and sintered at 1150 °C for 3 h (heating rate: 5 °C min^{-1}) in closed alumina crucibles. Selected samples were subjected to post-sintering aging at 120 °C in air for two weeks. Additionally, selected samples were coated with beta-tricalcium phosphate (β-TCP) using a dip-coating technique. For the dip-coating process, a slurry consisting of β-TCP powder, PVA binder, deionized water, and starch was prepared and thoroughly mixed until homogeneous. This slurry was applied to ceramic samples with $x = 0.15$. The samples were dipped and withdrawn at a constant speed, then dried at 120 °C for 24 h and calcined at 1000 °C for 1 h at a heating rate of 10 °C min^{-1}.

Bulk density was measured using Archimedes' method. Phase identification was performed using X-ray diffraction (XRD, RIGAKU, SMARTLAB), and Raman spectroscopy (T6400 JY, Horiba Jobin Yvon) was used to confirm structural features. Microstructure was examined using a scanning electron microscopy (SEM, JEOL JSM-6335F). Silver electrodes were applied to both sides of the samples and fired at 700 °C for 15 min. Dielectric properties were measured from 25 °C to 500 °C using an LCR meter (HP 4192A) at 1–1000 kHz. Polarization (P) and electrostrain (S) loops as a function of applied field (E) were recorded using a Radiant Precision High Voltage Interface at 25–150 °C, with $E = 50–95$ kV cm^{-1} at 1 Hz. From the measurements, energy storage density properties were calculated from the P–E hysteresis loop.

In vitro cytotoxicity was assessed using the MTT assay on human skin fibroblast cells obtained from Manose Health and Beauty Research Center (Thailand). The cells were cultured in DMEM with 10% FBS and 1% penicillin/streptomycin at 37 °C, 5% CO_2, and 100% humidity. Cultures were refreshed weekly, and the medium was replaced twice per week. Cells were treated with autoclaved bioceramic powders at concentrations of 0.1–1000 μg mL^{-1} for 24 h. Sodium lauryl sulfate (SLS) was used as a positive control. Absorbance was measured at 510 nm using a microplate reader. The bioactivity of the samples was also evaluated by immersing them in a simulated body fluid (SBF). Prior to testing, the samples were thoroughly cleaned to remove surface contaminants and then dried in an oven overnight to eliminate residual moisture. Each sample was immersed in 10 mL of phosphate-buffered saline (PBS, Sigma, Germany) with a pH of 7.4 and incubated in a temperature-controlled chamber at 37 ± 0.5 °C for 15 and 30 days to simulate biological conditions. The formation of apatite layers on the sample surfaces was subsequently examined using the scanning electron microscope.

3. Results and discussion

3.1 Densification and phase formation

To optimize densification, ceramics with varying STZ content were sintered at 1000–1175 °C, as shown in Fig. 1. All samples showed increased density with increasing temperature, reaching a maximum at 1150 °C and then decreasing at higher sintering temperatures. The decrease in density above 1150 °C is likely due to ion volatilization, particularly of Na^+ and Bi^{3+}.[35,36] Although 1150 °C was the optimal sintering temperature for all compositions, increasing STZ content reduced the maximum achievable density (inset of Fig. 1). Therefore, the densest ceramics, corresponding to the optimal sintering temperature for each composition, were selected for further investigation.

X-ray diffraction (XRD) patterns of the ceramics ($2\theta = 20–70°$, Fig. 2(a)) revealed a perovskite structure with coexisting rhombohedral (R) and tetragonal (T) phases. This was evidenced by peak splitting near $2\theta = 39–41°$ $((111)_R/(1\bar{1}1)_R)$ and 45–48° $((200)_T/(002)_T)$, as shown in Fig. S1 of the SI.[8,11,37] With

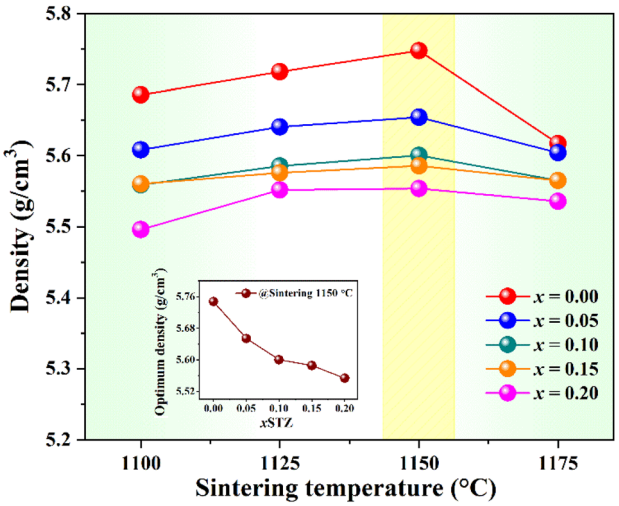

Fig. 1 Density of ceramics as a function of sintering temperature and composition. (Inset: relationship between optimal density and STZ content, *x*.)

increasing STZ content, the $(111)_R$ peak showed a slight change in shape, and the $\Delta 2\theta(200)$ ($\Delta 2\theta(200) = (2\theta_{(200)} - 2\theta_{(002)})$) value decreased, indicating reduced tetragonality (Fig. S2(a) in the SI). Furthermore, the relative tetragonality, expressed as the *c*/*a* ratio and calculated from the *d*-spacings of the (200) and (002) reflection planes, also decreased with increasing STZ content (Fig. S2(b) in the SI). These observations suggest that higher STZ concentrations diminish the tetragonal character of the material. Additionally, the XRD peaks shifted toward lower angles, indicating lattice expansion arising from the combined substitution of larger Zr^{4+} at the B-site and Sr^{2+} at the A-site. This distortion was further enhanced by the increased incorporation of Sr^{2+}, whose ionic radius is also larger than that of the host A-site ions.[20,23,38] This increased the average ionic radii at both A- and B-sites ($r_{A\text{-site}}$ and $r_{B\text{-site}}$), as shown in Fig. S3(a) in the SI. To evaluate the degree of lattice distortion, the tolerance factor (t) was calculated and found to increase with x, ranging from 0.717 to 0.9782 (Fig. S3(b) in the SI). This range falls within that typical of stable perovskite structures (t = 0.880–1.090).[39] However, an increase in the t reflects reduced symmetry distortion and a shift toward a more cubic structure, resulting in decreased tetragonality.

To quantify the phase fractions of rhombohedral (R) and tetragonal (T) phases in the samples, Rietveld refinement was performed using the GSAS-II software suite. The refinement results are illustrated in Fig. 2(b–f), providing visual confirmation of the phase evolution. Detailed numerical data from the refinement are compiled in Table S1 of the SI. All samples exhibited a mixture of phase composed of rhombohedral (*R3c*) and tetragonal (*P4bm*) phases. Notably, the proportion of the rhombohedral *R3c* phase increased with increasing STZ content. Conversely, the fraction of the tetragonal *P4bm* phase showed a corresponding decline, indicating a compositional shift driven by STZ incorporation. This trend aligns with the observed reduction in the *c*/*a* ratio.

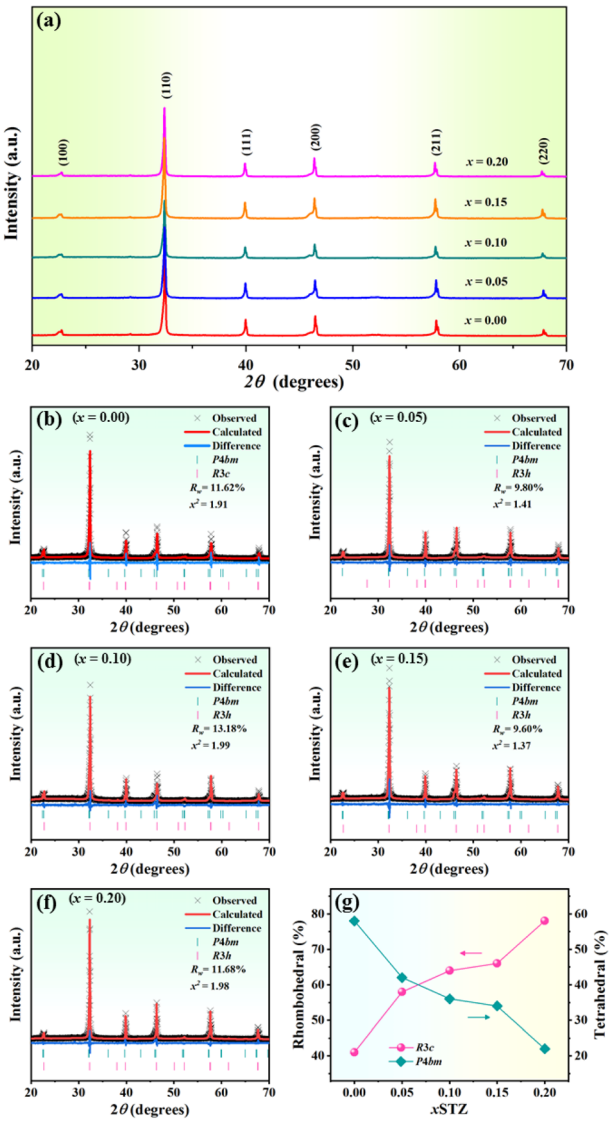

Fig. 2 (a) X-ray diffraction (XRD) patterns of samples with varying STZ content; (b–f) Rietveld refinement profiles for compositions x = 0.00 to 0.20; and (g) phase fractions of rhombohedral and tetragonal phases as a function of STZ content.

The Raman spectra (from 100–1000 cm^{-1}) of the ceramics were measured at room temperature (RT) and are presented in Fig. 3. The spectral deconvolution, performed using Lorentzian functions, identified seven modes (P1–P7), as described in Table S2 of the SI. The acquired spectra were divided into four distinct regions based on their Raman shift characteristics. The band below 200 cm^{-1} is closely correlated with the A-site cation vibrations of the perovskite structure, involving Na, Bi, and Sr ions.[40,41] The band between 200 and 400 cm^{-1} is related to the vibration of the Ti–O bond. This band exhibited a shift toward lower wavenumbers, which is likely attributed to distortions in the crystal lattice.[42,43] The band in the 430–700 cm^{-1} region corresponds to the vibrational modes of the TiO_6 octahedral units. This band became increasingly broadened as the x values rose, which may be linked to a higher degree of cation disorder.

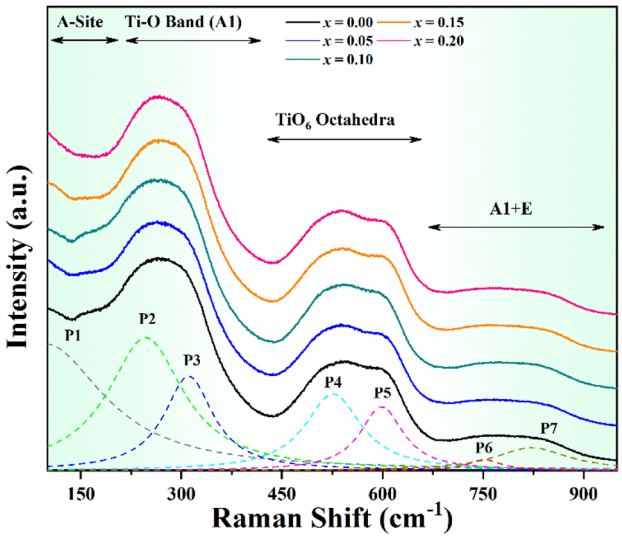

Fig. 3 Raman spectra of the ceramics at RT.

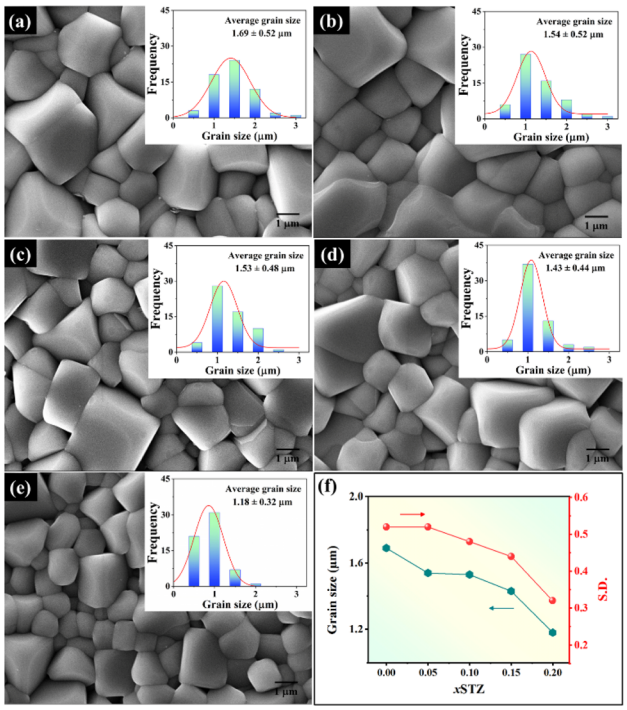

Fig. 4 SEM micrographs of (1 − *x*)[BNT–SBT]–*x*STZ ceramics: (a) $x = 0.00$, (b) $x = 0.05$, (c) $x = 0.10$, (d) $x = 0.15$, (e) $x = 0.20$; (f) average grain size and corresponding standard deviation as a function of *x*.

The high-frequency region above 700 cm^{-1} is associated with overlapping A_1 (longitudinal optical) and E (longitudinal optical) vibrational modes.[44,45] Therefore, the Raman results support the conclusions drawn from the XRD analysis.

3.2 Microstructure

The surface morphologies of the as-sintered ceramics were examined using scanning electron microscopy (SEM), as shown in Fig. 4. The corresponding fractured cross-sections are presented in Fig. S7. The average grain size and its distribution were quantified using the mean linear intercept method, as shown in the insets of Fig. 4. All compositions exhibited equiaxed grains with slightly rounded edges. Increasing the STZ content led to a systematic reduction in grain size, decreasing from 1.69 μm to 0.93 μm as *x* increased from 0.00 to 0.20. This grain refinement is likely associated with the incorporation of dopant ions into the BNT–SBT lattice, which introduces local lattice distortions and internal stresses that hinder grain boundary mobility during sintering.[46] In addition, according to the lattice strain energy expression (ΔG_{strain}), differences in ionic radii between the substituent and host ions can generate substantial strain energy, further suppressing grain growth. This strain energy can be quantified using the following expression:[47,48]

$$\Delta G_{strain} = 4\pi Y N_A[(r_0/2)(r_d - r_0)^2 + (1/3)(r_d - r_0)^3], \quad (1)$$

where *Y*, N_A, r_0, and r_d represent Young's modulus, Avogadro's number, the optimal radius of the host lattice site, and the ionic radius of the dopant, respectively. In this study, the higher concentration of Zr^{4+} ions (which possess a larger ionic radius than the B-site host ions) and the increased incorporation of Sr^{2+} ions, both of which have larger ionic radii than the respective B- and A-site host cations, can increase ΔG_{strain}. The elevated strain energy impedes grain boundary mobility and consequently suppresses grain growth. The grain-size distribution was monomodal across all samples, and the reduction in the standard deviation of the average grain size indicates improved grain uniformity with increasing STZ content (Fig. 4(f)).

Transmission electron microscopy (TEM) was performed on the $x = 0.00$ and $x = 0.15$ samples. The corresponding bright-field TEM images are presented in Fig. 5(a and b). Nanodomains in the $x = 0.00$ samples exhibited an average width of ~1.0 nm (highlighted by red boxes), while the $x = 0.15$ samples showed an average width of ~0.6 nm. The presence of nanodomains in both compositions suggests that the incorporation of SBT and STZ disrupts the long-range ferroelectric order in the studied ceramics, thereby promoting nanodomain formation. This disruption can induce an ergodic relaxor state, which is typically characterized by a slim *P–E* hysteresis loop, as discussed in Section 3.3.2.[19,49–51] For the $x = 0.00$ samples, the measured *d*-spacing was 0.2822 nm, corresponding to the (012) plane reflection, with weak $\frac{1}{2}$(ooo) superlattice reflections observed in the selected area electron diffraction (SAED) pattern (Fig. 5(c), inset), indicating a rhombohedral phase.[21,25] In contrast, the $x = 0.15$ sample exhibited *d*-spacings of 0.2770 nm and 0.2085 nm, corresponding to the (110) and (021) plane reflections, respectively, with no clear superlattice reflections observed in the SAED pattern (Fig. 5(d), inset). These observations are consistent with the XRD results.

3.3 Electrical properties

3.3.1 Dielectric properties and phase transition. Fig. 6 presents the dielectric constant (ε_r) and dielectric loss (tan δ) of

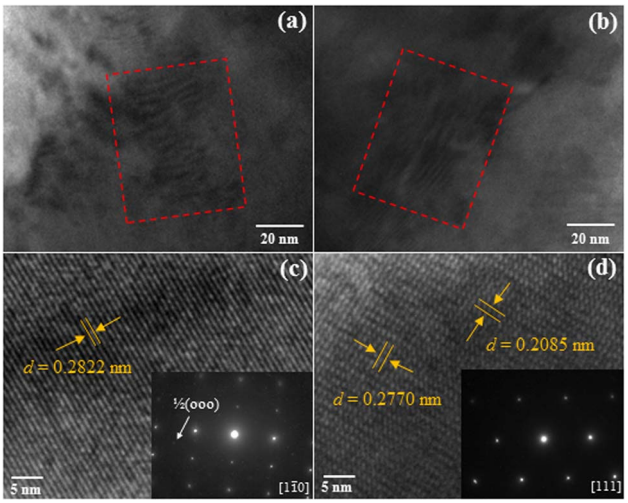

Fig. 5 (a and b) Bright-field TEM images of the $x = 0.00$ and $x = 0.15$ samples, respectively; (c and d) corresponding lattice fringe images for the $x = 0.00$ and $x = 0.15$ samples, with selected area electron diffraction (SAED) patterns shown in the insets.

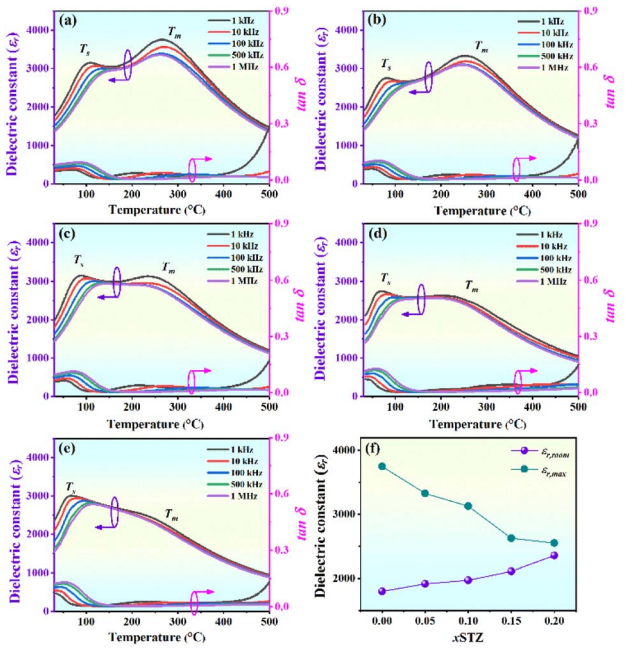

Fig. 6 Temperature dependence of the dielectric constant (ε_r) and dielectric loss (tan δ) of poled ceramics measured at various frequencies for different STZ compositions: (a) $x = 0.00$, (b) $x = 0.05$, (c) $x = 0.10$, (d) $x = 0.15$ and (e) $x = 0.20$. (f) Dielectric constant at RT ($\varepsilon_{r,room}$) and T_m ($\varepsilon_{r,max}$) as a function of STZ content (x).

the poled ceramics across various frequencies and temperatures. All samples exhibited two distinct dielectric anomalies in the ε_r–T curves, consistent with the behavior typically observed in BNT-based ceramics.[52,53] The first anomaly, marked by a dielectric peak at T_m (the temperature of maximum permittivity), corresponds to the relaxation of tetragonal polar nanoregions (PNRs) that emerge from rhombohedral PNRs.[8,54,55] With increasing STZ content, the temperature of the dielectric maximum (T_m) decreased from 268 °C at $x = 0.00$ to 222 °C at $x = 0.20$ (Fig. 7(a)). Moreover, the peak became broader and flatter as the STZ content (x) increased. The second anomaly, denoted as T_s, appeared below 100 °C and has been proposed to be attributed to the thermal evolution of discrete PNRs.[55,56]

The T_s decreased from 106 °C to 66 °C as x increased from 0.00 to 0.20 (Fig. 7(a)). The decrease in transition temperatures may be associated with the weakening of ionic bond strength caused by the STZ additive, which lowers the energy required for structural rearrangements and phase transitions.[57,58] Consequently, the reduced bond strength decreases the energy barrier for structural transformations, allowing phase transitions to occur at lower temperatures.[57] Additionally, this behavior correlates with the increase in the tolerance factor (t) at higher STZ contents, further supporting the lattice distortion induced by the additive.

In this study, the Burns temperature (T_B) was determined from the $1/\varepsilon_r$ *versus* T plot, as shown in Fig. S4 of the SI. T_B represents the temperature at which the dielectric constant begins to deviate from the Curie–Weiss law. As the STZ content increased, T_B exhibited a downward trend similar to that of T_m and T_s, decreasing from 394 °C at $x = 0.00$ to 326 °C at $x = 0.20$ (inset of Fig. 7(a)). This decrease in T_B with increasing STZ concentration reflects a progressive reduction in the onset temperature of polarization in the relaxor state.[52] Additionally, the incorporation of STZ increased the dielectric constant at room temperature ($\varepsilon_{r,room}$), which may be attributed to the downward shift of the T_s shoulder peak (Fig. 7(a)). However, the additive led to a reduction in the maximum dielectric constant ($\varepsilon_{r,max}$) at T_m (Fig. 6(f)), likely due to the broader of the ε_r–T curves observed with increasing STZ content.

It should be noted that as the STZ content increased, the dielectric constant (ε_r) near T_m decreased, and a plateau-like behavior became evident, suggesting improved thermal stability of the dielectric properties. To quantify this behavior, the temperature coefficient of capacitance (TCC) was calculated using the equation:[48,59]

$$\mathrm{TCC}\ (\%) = (\Delta\varepsilon/\varepsilon_b) \times 100\ (\%), \quad (2)$$

where $\Delta\varepsilon = \varepsilon_T - \varepsilon_b$, ε_T is the dielectric constant at evaluated temperature T, and ε_b is the dielectric constant at a base temperature (150 °C). A TCC ≤ 15% is generally considered indicative of good temperature stability. Fig. 7(b) illustrates the TCC as a function of temperature and STZ composition, while the corresponding temperature windows with TCC ≤ 15% are summarized in Fig. 7(c). As the STZ content increased, the TCC curves progressively flattened, indicating enhanced temperature stability, especially for the $x = 0.10$ and 0.15 samples. The temperature ranges where TCC values ≤ 15% for compositions $x = 0.00$, 0.05, 0.10, 0.15, and 0.20 were 71–226 °C, 49–210 °C, 51–323 °C, 38–310 °C, and 30–263 °C, respectively. Notably, the $x = 0.10$–0.15 compositions exhibited the highest temperature window, reaching 272 °C (inset of Fig. 7(c)). This value is considered high for lead free ceramics.[48,59]

It should be noted that, although the $x = 0.20$ composition exhibited a higher rhombohedral phase fraction at room

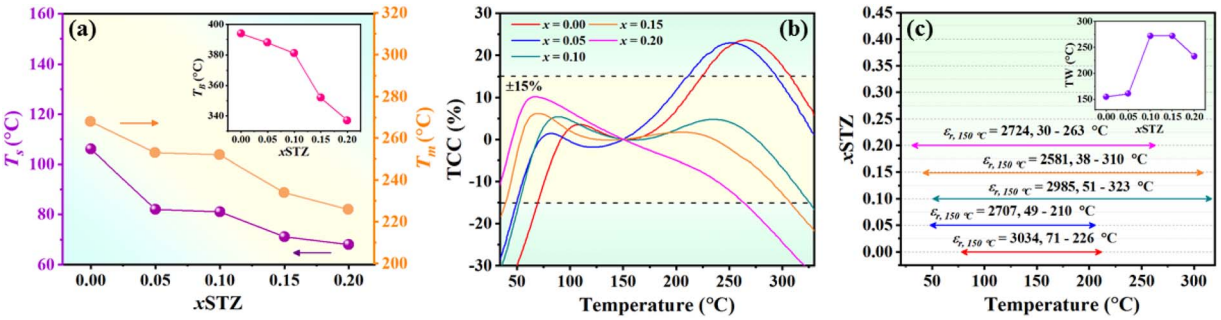

Fig. 7 (a) Variation of T_s and T_m with STZ composition (inset: T_B *versus* x); (b) TCC as a function of temperature and STZ content; (c) temperature window (TW) for TCC ≤ ±15% as a function of composition (inset: TW *versus* x).

temperature, it still showed a narrower TCC stability window. This behavior can be understood from the relaxor nature of the system. In BNT-based relaxors, the temperature stability of the dielectric constant is governed not by the static phase fraction at room temperature but by the thermal evolution of polar nanoregions (PNRs). Compositions within the phase coexistence region (x = 0.10–0.15) contain both rhombohedral and tetragonal local distortions, which create a flatter free energy landscape and enhance the thermal stability of PNR correlations. This structural competition suppresses abrupt temperature-driven fluctuations, allowing PNRs to respond more gradually to heating and thereby maintaining a stable permittivity over a broader temperature range. In contrast, the x = 0.20 composition lies outside the coexistence region, where a dominant rhombohedral distortion leads to softer lattice dynamics and reduced PNR stability. As a result, thermal depolarization occurs at lower temperatures, giving rise to a narrower TCC stability window. This explanation has been incorporated into the revised manuscript.

3.3.2 Ferroelectric and energy storage properties. Fig. 8(a–e) shows the *P–E* hysteresis loops of the ceramics at RT under 50 kV cm^{-1}. STZ doping significantly influences loop shape. The x = 0.00 samples exhibited a slim and pinched hysteresis loop, indicative of an ergodic relaxor state. As the STZ content increased, the loops became progressively slimmer. Additionally, both the maximum polarization (P_{max}) and remanent polarization (P_r) decreased with higher STZ levels (Fig. 8(f)). The coercive field (E_c) also decreased, consistent with the narrowing of the *P–E* hysteresis loops. These changes suggest that the addition of STZ enhances the ergodicity (Fig. 8(f)).[52] Furthermore, the observed trends can be further supported by broader *I–E* loops with increasing STZ content, as seen in Fig. 8(a–e),[60] which is often observed in BNT-based ceramics with high ergodicity. To compare the relative amount of the ergodic phase in the studied ceramic system, the parameter $(P_r/P_{max})A$ was used as an indicator, where A denotes the area of the *P–E* hysteresis loop. A value of $(P_r/P_{max})A$ approaching zero corresponds to a fully ergodic state. In this study, $(P_r/P_{max})A$ decreased with increasing x, indicating that the incorporation of STZ enhanced the ergodic character of the material.

Furthermore, temperature-dependent *P–E* hysteresis loops, as presented in Fig. S5 of the SI revealed that samples with x = 0.00–0.15 maintained slim, pinched shapes. In contrast, the pinched feature became less pronounced in the x = 0.20 samples, which exhibited only slim, non-pinched loops. Furthermore, as the temperature increased from 25 °C to 150 °C, all loops became progressively slimmer, indicating enhanced ergodic relaxor behavior due to thermal activation.[61]

In the current work, the energy storage density (W_{rec}) and energy storage efficiencies (η) of the studied ceramics were

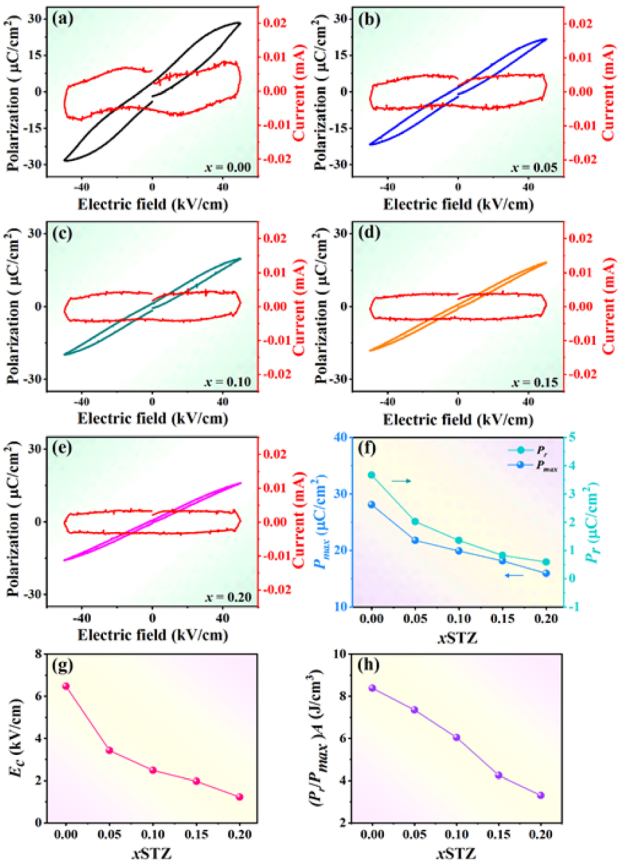

Fig. 8 (a–e) The *P–E* hysteresis loops and *I–E* loops of the ceramics for various STZ compositions, (f) variation of P_r and P_{max}, (g) E_c, and (h) $(P_r/P_{max})A$ as a function of x.

determined from the *P–E* hysteresis loops by using the following equations:[62–64]

$$W_{rec} = \int_{P_r}^{P_{max}} E\mathrm{d}P \quad (3)$$

$$\eta\ (\%) = \frac{W}{W_{rec} + W_{loss}} \times 100, \quad (4)$$

where E is the electric field and W_{loss} is the energy loss density. Plots of W_{rec} and η (at E = 50 kV cm^{-1}) as functions of composition (x) and temperature are presented in Fig. 9(a) and (b), respectively. At RT, the W_{rec} value showed a decreasing trend with increasing STZ content, while the η value exhibited an increasing trend. As the temperature rose to 150 °C, all samples displayed only minor changes in W_{rec} value, whereas the η value continued to increase. Notably, the samples with x = 0.15 seemed to exhibit the best thermal stability of W_{rec}, while x = 0.20 showed the greatest thermal stability of η.

To assess the thermal stability of W_{rec}, its temperature dependence was evaluated using the following equation,[62,65] and the results are presented in Fig. 9(c).

$$\frac{\Delta W_T}{W_{25°C}} = \frac{|W - W_{25°C}|}{W_{25°C}} \times 100, \quad (5)$$

where $W_{25°C}$ is the energy storage density at 25 °C, W_T is the energy storage density at the measured temperature (ranging from 25 °C to 125 °C), and ΔW_T represents the difference between W_T and $W_{25°C}$. Additionally, the temperature stability of η was evaluated using the following equation, and the results are presented in Fig. 9(d).

$$\frac{\Delta \eta}{\eta_{25°C}} = \frac{|\eta - \eta_{25°C}|}{\eta_{25°C}} \times 100, \quad (6)$$

where $\eta_{25°C}$ is the energy storage efficiency at 25 °C, η_T is the efficiency at the measured temperature (25–125 °C), and $\Delta\eta_T$ represents the difference between η_T and $\eta_{25°C}$. Based on the calculation, the x = 0.15 and x = 0.20 samples exhibited $\Delta W_T/W_{25°C}$ of 1.48% and 3.17%, respectively. Additionally, they showed energy efficiency stability values $\Delta\eta/\eta_{25°C}$ of 12.69% and 6.10%, respectively. These values demonstrate relatively strong performance when compared to other BNT-based ceramics reported in the literature, such as $0.90Bi_{0.5}Na_{0.5}TiO_3BaTiO_3$–$0.10NaNbO_3$ (W_{rec} = 0.71 J cm^{-3}, $\Delta W_T/W_{25°C}$ < 12% (25–150 °C)),[66] $0.8BaTiO_3$–$0.15Bi(Y_{1/3}Ti_{1/2})O_3$ (W_{rec} = 1.02 J cm^{-3} and $\Delta W_T/W_{25°C}$ = 18% (25–125 °C)),[65] and $0.98Bi_{0.5}Na_{0.5}TiO_3$–$0.06BaTiO_3$–$0.02Sr_{0.8}Na_{0.4}Nb_2O_6$–$0.20NaNbO_3$ (W_{rec} = 1.52 J cm^{-3}, $\Delta W_T/W_{25°C}$ < 8.70% (RT–160 °C)).[67] This suggests that the incorporation of STZ significantly enhances the thermal stability of the ceramic system.

The effect of the applied electric field on W_{rec} and η values (at 125 °C) was also investigated in this study (Fig. 9(e) and (f)). Notably, all samples exhibited the highest η value at 125 °C; therefore, the analysis focused on this temperature. As the electric field increased, W_{rec} showed a clear upward trend (Fig. 9(e)), while η exhibited only slight variations (Fig. 9(f)). The W_{rec} and η values measured at 125 °C, along with the ceramics' breakdown strength (E_b) as a function of x, are shown in Fig. 9(h). The W_{rec} value increased with increasing x, reaching a maximum of 1.01 J cm^{-3} for the x = 0.15 samples. Furthermore, η increased from 85.80% for the x = 0.00 samples to 91.25% for the x = 0.15 samples. It is important to highlight that beyond x = 0.05, η remained relatively stable, varying only slightly between 91.25% and 92.90%. These results indicate that STZ enhances both W_{rec} and η, with minimal variation in η for x between 0.05 and 0.20 (at 125 °C). In addition, the trend of W_{rec} value closely aligns with that of the E_b value, as illustrated in Fig. 9(g) and (h). This correlation is consistent with the well-established understanding that a higher E_b typically leads to a higher W_{rec}, as elevated E_b values are often associated with finer grain sizes.[3,68] However, the lower W_{rec} observed in the x = 0.20 sample can be attributed to the dominant influence of porosity. It is well known that increased porosity (*i.e.*, lower

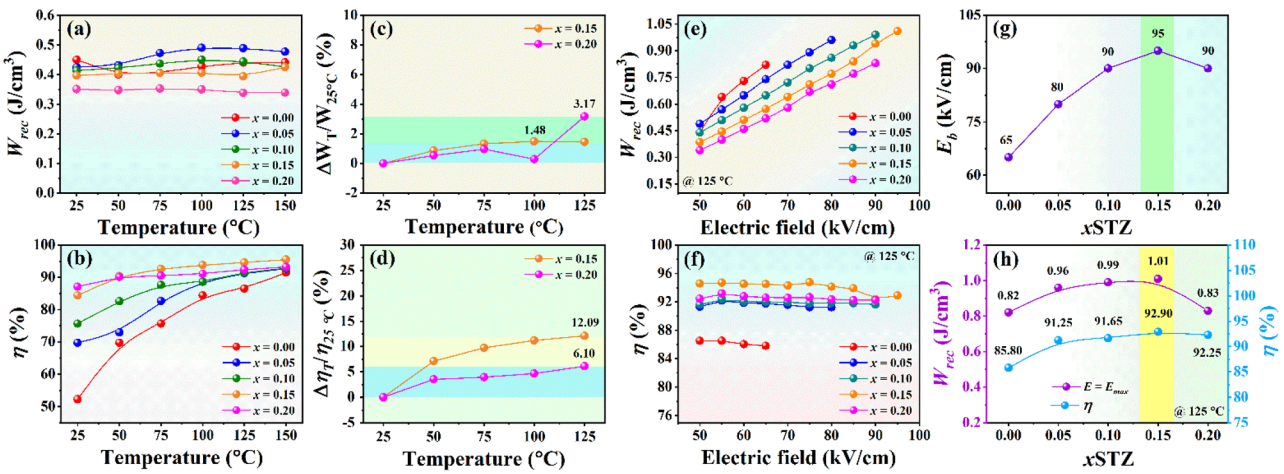

Fig. 9 Energy storage properties of the ceramics: (a) W_{rec} *versus* temperature at 50 kV cm^{-1}, (b) η *versus* temperature at 50 kV cm^{-1}, (c) $\Delta W_T/W_{25°C}$ as a function of temperature at 50 kV cm^{-1}, (d) change in $\Delta\eta/\eta_{25°C}$ with temperature at 50 kV cm^{-1}, (e) W_{rec} *versus* electric field for various x and at 125 °C and (f) η *versus* electric field for various x and at 125 °C, (g) breakdown strength (E_b) for various x, and (h) W_{rec} and η *versus* x at 125 °C and at their E_b.

density) in ceramics tends to reduce E_b, thereby resulting in a lower W_{rec}.[2,3,69–71]

In this work, the enhanced electrical properties of the studied ceramics arise from STZ-induced modifications to the coexistence and the resulting evolution of lattice and domain structures. XRD Rietveld analysis shows that increasing STZ progressively shifts the phase assemblage toward a more rhombohedral character while reducing tetragonality, indicating MPB tuning that facilitates easier polarization rotation. Complementary Raman softening and band broadening further reveal increased lattice distortion and cation disorder, consistent with a softened lattice and the suppression of long-range ferroelectric order. TEM observations confirm that macroscopic ferroelectric domains are fragmented into finer nanodomains (from ~1.0 nm to ~0.6 nm), demonstrating the development of polar nanoregions (PNRs) that govern the relaxor behavior. This structural transformation results in broadened dielectric anomalies, reduced P_r and E_c, and slimmer *P–E* loops, which collectively promote high energy-storage efficiency and excellent thermal stability. Additionally, STZ-induced grain refinement enhances dielectric breakdown strength, further increasing the recoverable energy density (W_{rec}).

Among all investigated compositions, $x = 0.15$ STZ demonstrated the optimum in dielectric and energy-storage performance, owing to its optimal synergy of phase structure, microstructure, dielectric relaxation, and electrical strength. XRD-Rietveld and Raman analyses revealed that this composition achieved the most balanced rhombohedral–tetragonal coexistence together with higher degree of local structural disorder (Fig. 2 and 3), fostering a pronounced relaxor state. TEM observations confirmed the presence of nanodomains (~0.6 nm), which enable highly reversible polarization switching and yield slim *P–E* loops with low remanent polarization (P_r) and minimal energy loss (Fig. 8). SEM analysis further showed that $x = 0.15$ possessed the smaller and more uniform grains, resulting in the highest E_b (Fig. 9), which directly enhances the recoverable energy density (W_{rec}). Consequently, this composition delivered the maximum W_{rec} ($\approx$1.01 J cm^{-3}) with a high efficiency of 92.9% (Fig. 9). In addition, it exhibited one of the broadest temperature-stable dielectric windows (TCC $\leq \pm$15%), ensuring a reliable dielectric constant across a wide operating range (Fig. 7). Taken together, these structural and electrical merits establish $x = 0.15$ as the optimal STZ concentration.

3.3.3 Strain behavior. Since the $x = 0.15$ composition exhibited the optimal W_{rec} and η, its electrostrain behaviour was further investigated. Fig. 10(a) displays the bipolar strain–electric field (*S–E*) curves for the $x = 0.15$ samples. The samples exhibited a slim loop with a very low maximum strain (S_{max}) of 0.06%. This corresponds to the slim and pinched shape of the *P–E* hysteresis loop (Fig. 10(b)). This behavior is indicative of a dominant ergodic relaxor (ER) phase in the $x = 0.15$ samples. To enhance the strain response, the $x = 0.15$ samples underwent a post-sintering aging treatment at 120 °C for two weeks. After aging, the strain performance improved significantly, with the maximum strain increasing to 0.33%, representing a 450% enhancement. To ensure statistically reliable strain measurements, the *P–E* and *S–E* loops were recorded three times. Before annealing, the average strain was 0.05%, whereas after annealing, it increased to 0.31% (see Fig. S10 in the SI). Furthermore, the normalized strain coefficient d^*_{33} ($d^*_{33} = S_{max}/E_{max}$) increased from 100 pm V^{-1} in the unaged samples to 550 pm V^{-1} in the aged samples, also reflecting a 450% improvement. In addition, the degree of strain hysteresis (H) was calculated using the equation: $H = \frac{\Delta S_{E_{max}/2}}{S_{max}} \times 100\%$, where $\Delta S_{E_{max}/2}$ represents the strain deviation during the application and removal of the electric field, measured at half of the maximum electric field.[72,73] The H value significantly improved after aging, changing from 29.50% in the unaged samples to 18.09% in the aged samples, which represents an improvement of 63.07%.

Many authors have proposed that the significant strain enhancement observed after post-sintering treatments arises from several mechanisms, most notably the generation and redistribution of oxygen vacancies. These vacancies can form defect-dipole complexes that interact with polar nanoregions, facilitating field-induced ordering and thereby increasing the strain response.[74,75] To verify this, electron paramagnetic resonance (EPR) spectroscopy was conducted, and the resulting data are presented in Fig. 10(c). The aged samples exhibited a strong resonance signal at approximately $g = 2.06$, which is consistent

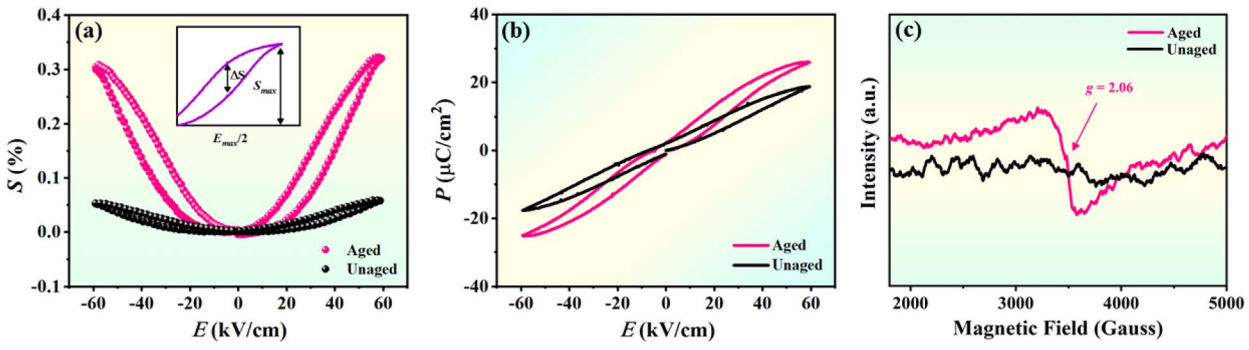

Fig. 10 Strain behavior of 0.15 composition for unaged and aged samples under an electric field of 60 kV cm^{-1}: (a) bipolar *S–E* loops, (b) *P–E* hysteresis loops and, (c) EPR signal (inset: definition of the degree of strain hysteresis using $H = (\Delta S_{E_{max}/2})/S_{max}$ at 1 Hz).

with the typical EPR signal of oxygen vacancies, while the unaged sample showed no detectable signal.[74] This EPR signal in the aged samples may indicate the presence of oxygen vacancies. However, the samples were aged at a relatively low temperature (120 °C), which may not be high enough to thermally generate additional oxygen vacancies beyond those already present from sintering. Therefore, X-ray photoelectron spectroscopy technique (XPS) was employed to confirm the EPR result, and the obtained results are displayed in Fig. S11 in SI. The obtained XPS data revealed that there was no significant change in concentration of oxygen vacancies. Therefore, aging may not affect to produce the oxygen vacancy concentration. This evidence can be explained as the following. Normally, oxygen vacancies are expected to form during the high-temperature sintering of BNT-based ceramics because volatilization of Bi and Na components, creating A-site vacancies, which are compensated by the formation of oxygen vacancies to maintain charge neutrality. Furthermore, heterovalent substitution, such as Sr^{2+} replacing Bi^{3+}/Na^{+}, creates charge imbalance and leads to oxygen vacancy formation during sintering. However, the oxygen vacancies produced during sintering are usually very mobile and can hop rapidly between neighboring oxygen lattice sites. Because they do not remain at one position long enough, they cannot form a stable paramagnetic center that EPR can detect. In many cases, the associated electrons are also electronically delocalized, meaning they spread over a wider region of the lattice instead of being trapped at a single vacancy. Another possibility is that the vacancies become part of charge-neutral defect complexes, for example, a combination of an A-site vacancy and an oxygen vacancy, and such complexes do not contain any unpaired electron.[76] As a result, the oxygen vacancies present after sintering do not generate an EPR signal. Because none of these configurations produces a localized magnetic moment, the vacancies remain EPR-silent in the unaged state.[76] During aging at 120 °C in air, the pre-existing oxygen vacancies can move slightly and become linked with nearby cations. When this happens, the vacancy can trap electrons and form occupied in-gap states. These localized electrons create paramagnetic centers that can be detected by EPR.[77] Because oxygen re-incorporation is negligible at 120 °C, aging stabilizes oxygen vacancies, causing EPR signals to appear only after aging.

Although the aging treatment at 120 °C does not generate additional oxygen vacancies, it enables the pre-existing vacancies formed during sintering to migrate, associate with cation defects, and align into stable defect-dipole configurations.[78] In the studied ceramics with a dominant ergodic relaxor phase, the oriented defect dipoles interact strongly with the dynamic polar nanoregions (PNRs). Their alignment generates local internal bias fields that partially steer the orientation of adjacent PNRs, modify the local energy landscape, and promote specific polarization directions. When an electric field is applied, this interaction promotes the field-induced transformation of the ergodic relaxor into a temporary ferroelectric-like state. Importantly, once the field is removed, the defect-dipole-induced internal bias acts as a restoring force, driving the PNRs to collapse back into the ergodic relaxor phase in a highly reversible manner.[79,80] This may improve reversibility of the electric field driven relaxor to ferroelectric transition leads to a substantial increase in recoverable electrostrain. Therefore, the large electrostrain enhancement from 0.06% to 0.33% originates from vacancy reorganization and dipole alignment, not from an increase in vacancy concentration.

3.4 Bioactivities

Recently, there has been growing attention toward the application of piezoelectric materials, particularly lead-free piezoceramics, in the medical field. As a result, understanding their biological characteristics has become increasingly significant.[30,81,82] In this study, we investigated the bioactivity of the $x = 0.15$ samples to evaluate their potential for biomedical use.

3.4.1 *In vitro* cell viability assay. Cell viability assays are commonly used to determine whether cells remain alive or undergo cell death following exposure to a drug or chemical, which is essential for evaluating the safety of materials intended for biomedical applications. In this study, the MTT assay, a colorimetric method, was employed to assess cell viability. Human skin fibroblast cells (Manose Health and Beauty Research Center) were used for testing, with sodium lauryl sulfate (SLS) serving as a positive control. The *in vitro* cell viability results for the $x = 0.15$ samples are shown in Fig. 11(a). The results revealed no significant morphological changes, such as cell wall shrinkage or bulging, across all tested concentrations ranging from 0.1 to 1000 μg ml^{-1}. In the current work, the cell viability was quantified by comparing the absorbance of cells treated with the sample suspensions to that of cells exposed only to the culture medium (control), using the following formula:[83]

$$\text{Cell viability } (\%) = \frac{\text{absorbance}_{\text{ceramics}}}{\text{absorbance}_{\text{control}}} \times 100 \quad (7)$$

The results showed that the $x = 0.15$ samples maintained cell viability above 95% across all tested concentrations (0.1–1000 μg ml^{-1}), as illustrated in Fig. 11(b). Compared to previous

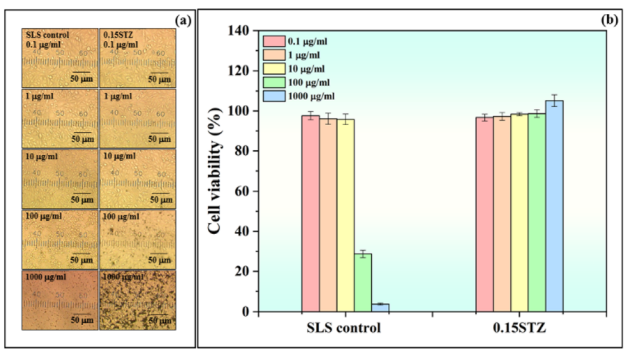

Fig. 11 (a) Optical images showing the survival of cells treated for the $x = 0.15$ ceramics at various concentrations (100x) and (b) the corresponding histogram illustrating the percentage of cell viability. The experiment was performed using an Olympus CK40 optical microscope (Tokyo, Japan) with 6 V, 30 W HAL (halogen) illumination (Philips 5761).

studies, these results show noticeably higher values (Table S3 in the SI).[84–88] This also indicates that the samples are non-toxic and may support cell growth, which is essential for their intended biomedical applications.

3.4.2 ***In vitro*** **bone-like apatite formation.** The formation of bone-like apatite in simulated body fluid (SBF) is widely recognized as a key indicator of bioactivity, reflecting a material's potential to bond with surrounding biological tissues. In this study, the $x = 0.15$ samples were immersed in SBF for 15 and 30 days, and the results are presented in Fig. 12. After 15 days of immersion, no apatite formation was observed on the sample surfaces (Fig. 12(b)). However, after 30 days, small precipitated apatite particles, with an average size of approximately 0.08 μm, were detected, partially covering the surface (Fig. 12(c)). The formation of apatite particles was confirmed using energy-dispersive spectroscopy (EDS), as shown in Fig. S6 of the SI. The formation of apatite may be related to the release of mobile cations such as Na^+, Bi^{3+}, and Sr^{2+} from grain boundaries or defect sites during immersion. This release can result in a cation-depleted surface with a net negative charge. Such a local charge environment attracts Ca^{2+} and PO_4^{3-} ions from the simulated body fluid (SBF) and increases the local pH, both of which are favorable for calcium phosphate precipitation. These released ions help modify the surrounding chemical environment, thereby promoting apatite nucleation from the calcium and phosphate species present in SBF.[89] Furthermore, immersion in SBF can lead to surface hydroxylation of the ceramics, forming –OH groups such as Ti–OH or Zr–OH that act as nucleation sites for calcium phosphate.[90]

However, the delayed appearance of apatite in the $x = 0.15$ composition (compared with the coated samples) can be attributed to its lower initial surface reactivity. The incorporation of the STZ component may reduce the surface energy of the ceramics, thereby slowing the early stages of apatite nucleation,[91] weakening interactions with ionic species in SBF and slowing the formation of Ca–P nuclei. Furthermore, Zr^{4+} substitution alters the local BO_6 octahedral environment and may suppress dissolution-driven cation release, limiting the early development of a negatively charged, Ca^{2+}-attracting surface. The generation of surface –OH groups also proceeds more gradually at this composition, reducing Ca^{2+} adsorption during the early stage of immersion. Collectively, these factors delay the surface activation process, resulting in apatite becoming detectable only after extended soaking (30 days).

To enhance apatite formation, samples with $x = 0.15$ were coated with β-tricalcium phosphate (β-TCP) using a dip-coating technique, as β-TCP is a well-known bioactive material. The coated surface exhibited a rounded grain morphology with an average grain size of 0.88 μm and a coating thickness of approximately 176 μm (Fig. 12(d)). After 15 days of SBF immersion, apatite particles with an average size of ~0.08 μm were observed on the coated samples, although they did not fully cover the surface (Fig. 12(e)). After 30 days of immersion, the coated samples exhibited extensive apatite formation, characterized by larger flake-like precipitates approximately 0.17 μm in width and less than 0.03 μm in thickness (Fig. 12(f)). These precipitates covered a greater portion of the surface and formed larger clusters compared to those observed on the 15-day samples. Compared to the uncoated samples, the β-TCP coating significantly enhanced apatite formation, likely due to the release of Ca^{2+} and PO_4^{3-} ions, which are essential for apatite development and contribute to the formation of a continuous apatite layer.[92]

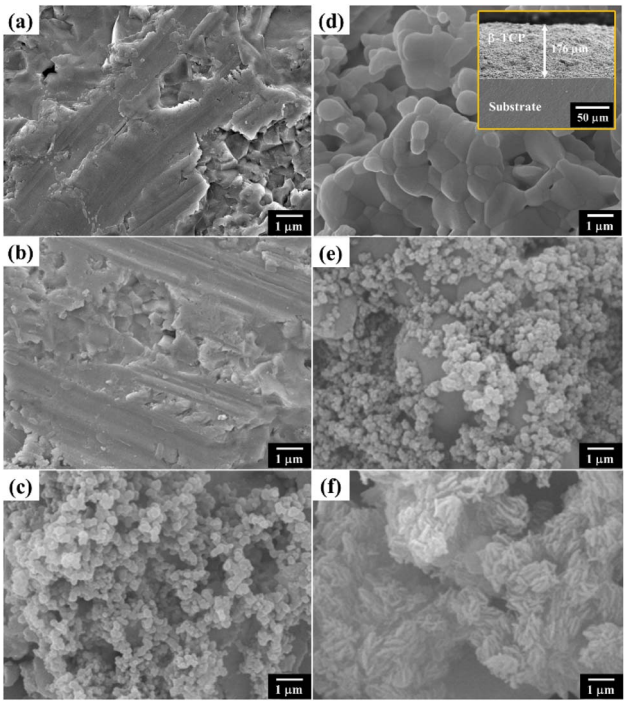

Fig. 12 SEM images of the $x = 0.15$ samples before and after immersion in SBF: (a) uncoated sample before SBF immersion, (b) uncoated sample after 15 days in SBF, (c) uncoated sample after 30 days in SBF, (d) β-TCP-coated sample before SBF immersion (inset: cross-sectional SEM image showing a coating thickness of ~176 μm), (e) β-TCP-coated sample after 15 days, and (f) β-TCP-coated sample after 30 days in SBF.

4. Conclusions

The $(1 - x)$[BNT–SBT]–xSTZ ceramics were synthesized *via* a conventional solid-state reaction route. All compositions demonstrated coexistence of rhombohedral and tetragonal phases, with a progressive reduction in tetragonality as the STZ content increased. Notably, the $x = 0.15$ composition exhibited optimum dielectric and energy storage characteristics, including the highest TCC, optimized W_{rec}, η, and enhanced E_b. This composition also showed excellent thermal stability of W_{rec}, despite a relatively low initial strain response. Following aging treatment, the $x = 0.15$ samples exhibited a remarkable 450% increase in S_{max} and d_{33}^* values, emphasizing the role of aging in boosting electromechanical performance. This enhancement likely originates from the reorganization of pre-existing oxygen vacancies into aligned defect dipoles rather than from an increase in vacancy concentration. The MTT assay results demonstrated good cell viability for the $x = 0.15$ composition, indicating favorable biocompatibility.

Furthermore, SBF immersion tests indicated moderate bioactivity for the $x = 0.15$ samples. Consequently, bioactivity was markedly enhanced following the application of β-TCP surface coating, highlighting its beneficial role in promoting the biological response. These results collectively underscore the promising potential of the $x = 0.15$ ceramics for future biomedical applications.

Author contributions

Kamonporn Saenkam: writing – original draft, validation, methodology, investigation. Waraporn Boontakam: methodology, investigation. Phanrawee Sriprapha: methodology, investigation. Pichitchai Butnoi: methodology, investigation. Kamonpan Pengpat: supervision, conceptualization, methodology, formal analysis. Chamnan Randorn: supervision, conceptualization, methodology, formal analysis. Gobwute Rujijanagul: writing – review & editing, conceptualization, supervision, formal analysis, methodology, investigation, supervision project administration.

Conflicts of interest

There are no conflicts to declare.

Data availability

The data supporting this article have been included as part of the supplementary information (SI). Supplementary information is available. See DOI: https://doi.org/10.1039/d5ra07450a.

Acknowledgements

This project was supported by the Materials Science Research Center (Fundamental Fund 2025, Chiang Mai University), Chiang Mai University. We also acknowledge the Office of Research Administration, the Department of Physics and Materials Science, Faculty of Science, the Multidisciplinary Research Institute, Chiang Mai University for their contributions, and Science and Technology Research Grant (STRG) Thailand Toray Science Foundation (the 31st Science and Technology Research Grant, 2024).

References

1 J. Hao, W. Li, J. Zhai and H. Chen, *Mater. Sci. Eng., R*, 2019, **135**, 1–57.
2 X. Zhou, G. Xue, H. Luo, C. R. Bowen and D. Zhang, *Prog. Mater. Sci.*, 2021, **122**, 100836.
3 G. Wang, Z. Lu, Y. Li, L. Li, H. Ji, A. Feteira, D. Zhou, D. Wang, S. Zhang and I. M. Reaney, *Chem. Rev.*, 2021, **121**, 6124–6172.
4 X. Zhang, D. Hu, Z. Pan, X. Lv, Z. He, F. Yang, P. Li, J. Liu and J. Zhai, *Chem. Eng. J.*, 2021, **406**, 126818.
5 L. Li, P. Fan, M. Wang, N. Takesue, D. Salamon, A. N. Vtyurin, Y. Zhang, H. Tan, B. Nan, Y. Lu, L. Liu and H. Zhang, *J. Phys. D: Appl. Phys.*, 2021, **54**, 293001.
6 P. Jaita, K. Saenkam and G. Rujijanagul, *RSC Adv.*, 2023, **13**, 3743.
7 B. Jaffe, W. R. Cook Jr. and H. Jaffe, *Piezoelectric Ceramics*, Academic Press, London and New York, 1971.
8 R. F. Ge, Z. H. Zhao, S. F. Duan, X. Y. Kang, Y. K. Lv, D. S. Yin and Y. Dai, *J. Alloys Compd.*, 2017, **724**, 1000–1006.
9 P. Fan, Y. Zhang, B. Xie, Y. Zhu, W. Ma, C. Wang, B. Yang, J. Xu, J. Xiao and H. Zhang, *Ceram. Int.*, 2018, **44**, 3211–3217.
10 Y. Hiruma, H. Nagata and T. Takenaka, *Appl. Phys. Lett.*, 2009, **95**, 052903.
11 K. Wang, A. Hussain, W. Jo and J. Rödel, *J. Am. Ceram. Soc.*, 2012, **95**, 1–7.
12 S. T. Zhang, A. B. Kounga and E. Aulbach, *Appl. Phys. Lett.*, 2007, **91**, 112906.
13 P. Jaita, R. Sanjoom and G. Rujijanagul, *Mater. Res. Bull.*, 2023, **167**, 112417.
14 J. Shi, H. Fan, X. Liu and A. J. Bell, *J. Am. Ceram. Soc.*, 2014, **97**, 848–853.
15 S. Manotham, P. Jaita, C. Randorn, G. Rujijanagul and D. P. Cann, *J. Alloys Compd.*, 2019, **808**, 151655.
16 V. Veerapandiyan, F. Benes, T. Gindel and M. Deluca, *Materials*, 2020, **13**, 5742.
17 X. Zhou, H. Qi, Z. Yan, G. Xue, H. Luo and D. Zhang, *ACS Appl. Mater. Interfaces*, 2019, **11**, 43107–43115.
18 X. Liu, H. Du, X. Liu, J. Shi and H. Fan, *Ceram. Int.*, 2016, **42**, 17876–17879.
19 X. Zhou, H. Qi, Z. Yan, G. Xue, H. Luo and D. Zhang, *J. Eur. Ceram. Soc.*, 2019, **39**, 4053–4059.
20 X. Qiao, D. Wu, F. Zhang, M. Niu, B. Chen, X. Zhao, P. Liang, L. Wei, X. Chao and Z. Yang, *J. Eur. Ceram. Soc.*, 2019, **39**, 4778–4784.
21 H. Qi and R. Zuo, *J. Mater. Chem. A*, 2019, **7**, 3971–3978.
22 W. Ma, Y. Zhu, M. A. Marwat, P. Fan, B. Xie, D. Salamon, Z. G. Ye and H. Zhang, *J. Mater. Chem. C*, 2019, **7**, 281.
23 D. Li, Y. Lin, M. Zhang and H. Yang, *Chem. Eng. J.*, 2020, **392**, 123729.
24 C. Ang and Z. Yu, *Appl. Phys. Lett.*, 2009, **95**, 232908.
25 D. Wang, B. Chu, P. Li, W. Han, Y. Kong, P. Fu, Y. Li, J. Hao and W. Li, *Ceram. Int.*, 2023, **49**, 37486–37493.
26 S. Parida, S. K. Rout, V. Subramanian, P. K. Barhai, N. Gupta and V. R. Gupta, *J. Alloys Compd.*, 2012, **528**, 126–134.
27 J. R. Quiñones-Gurrola, J. C. Rendón-Angeles, Z. Matamoros-Veloza, J. López-Cuevas, R. Pérez-Garibay and K. Yanagisawa, *Nanomaterials.*, 2023, **13**, 2195.
28 C. Ostos, M. L. Martínez-Sarrión, L. Mestres, E. Delgado and P. Prieto, *J. Solid State Chem.*, 2009, **182**, 2620–2625.
29 C. Ostos, L. Mestres, M. L. Martínez-Sarrión, J. E. Garcı, A. Albareda and R. Perez, *Solid State Sci.*, 2009, **11**, 1016–1022.
30 A. Das and D. Pamu, *Mater. Sci. Eng., C*, 2019, **101**, 539–563.
31 N. A. Kamel, *Biophys. Rev.*, 2022, **14**, 717–733.
32 A. K. Dubey, R. Kinoshita and K. Kakimoto, *RSC Adv.*, 2015, **5**, 19638–19646.
33 S. Phromyoo, N. Lertcumfu, P. Jaita, P. Jarupoom, K. Pengpat and G. Rujijanagul, *Ceram. Int.*, 2018, **44**, 2661–2667.
34 N. Lertcumfu, P. Jarupoom and G. Rujijanagul, *Ceram. Int.*, 2013, **39**, S373–S377.

35 A. J. Moulson and J. M. Herbert, *Electroceramics: Materials, Properties, Applications*, John Wiley & Sons Ltd, 2nd edn, 2003.
36 J. U. Rahman, A. Hussain, A. Maqbool, R. A. Malik, M. S. Kim and M. H. Kim, *J. Korean Phys. Soc.*, 2015, **66**, 1072–1076.
37 M. R. Bafandeh, H. S. Han and J. S. Lee, *J. Electroceram.*, 2021, **47**, 89–99.
38 F. Akram, M. Sheeraz, A. Hussain, I. W. Kim, T. H. Kim and C. W. Ahn, *Ceram. Int.*, 2021, **47**, 23488–23496.
39 J. Wu, H. Zhang, N. Meng, V. Koval, A. Mahajan, Z. Gao, D. Zhang and H. Yan, *Mater. Des.*, 2021, **198**, 109344.
40 J. Wang, C. Zhou, Q. Li, W. Zeng, J. Xu, G. Chen, C. Yuan and G. Rao, *J. Mater. Sci.*, 2018, **53**, 8844–8854.
41 S. Manotham, P. Jaita, P. Butnoi, N. Lertcumfu and G. Rujijanagul, *J. Alloys Compd.*, 2022, **897**, 163021.
42 L. Li, C. Zhou, D. Yu, Y. Zheng, Y. Du, L. Ma, J. Zhao and G. Rao, *J. Electron. Mater.*, 2023, **52**, 3488–3498.
43 Q. Xu, X. Yan, Z. Zhu and H. Liu, *Process. Appl. Ceram.*, 2023, **17**, 400–409.
44 B. Yan, H. Fan, A. K. Yadav, C. Wang, Z. Du, M. Li, W. Wang, W. Dong and S. Wang, *J. Mater. Sci.*, 2020, **55**, 14728–14739.
45 R. A. Malik, A. Hussain, A. Zaman, A. Maqbool, J. U. Rahman, T. K. Song, W. J. Kimc and M. H. Kim, *RSC Adv.*, 2015, **5**, 96953–96964.
46 G. M. Rashwan, A. A. Ebnalwaled, E. M. Saad and M. A. Shahat, *J. Sol-Gel Sci. Technol.*, 2024, **109**, 707–719.
47 X. Gong, C. Zhang, D. Su, W. Xiao, F. Cen, Y. Yang, S. Jiang, J. Wang, K. Li and G. Zhang, *J. Materiomics*, 2024, **10**, 1196–1205.
48 N. Qin, X. Chen, L. Liu, L. Tian and Z. Liu, *J. Mater. Sci.: Mater. Electron.*, 2025, **36**, 262.
49 P. Jaita, S. Manotham and G. Rujijanagul, *RSC Adv.*, 2020, **10**, 32078.
50 C. Che, Y. Bao, Z. Hu, Q. Feng, M. Xie, B. Zhou, J. Yang, H. Nie, Z. Gao and G. Wang, *J. Mater. Chem. C*, 2024, **12**, 16732.
51 Q. Xu, J. Xie, Z. C. He, L. Zhang, M. H. Cao, X. D. Huang, M. T. Lanagan, H. Hao, Z. H. Yao and H. X. Liu, *J. Eur. Ceram. Soc.*, 2017, **37**, 99–106.
52 S. K. Gupta, R. M. Quade, B. Gibbons, P. Mardilovich and D. P. Cann, *J. Appl. Phys.*, 2020, **127**, 074104.
53 Q. Wei, M. Zhu, T. Qin, Z. Guo, M. Zheng, Y. Hou, H. Liu and J. Chen, *RSC Adv.*, 2018, **8**, 12269–12275.
54 G. Liu, J. Dong, L. Zhang, Y. Yan, R. Jing and L. Jin, *J. Materiomics*, 2020, **6**, 677–691.
55 M. Wang, Q. Feng, Y. Wei, N. Luo, C. Yuan, C. Zhou, T. Fujita, J. Xu and G. Chen, *J. Phys. Chem. Solids*, 2021, **157**, 110209.
56 X. S. Qiao, X. M. Chen, H. L. Lian, W. T. Chen, J. P. Zhou and P. Liu, *J. Am. Ceram. Soc.*, 2016, **99**, 198–205.
57 J. H. Kim, D. H. Kim, T. H. Lee, T. G. Lee, J. H. Lee, B. Y. Kim, S. Nahm, C. Y. Kang and J. Ryu, *J. Am. Ceram. Soc.*, 2016, **99**, 1–8.
58 K. Singh, S. Acharya and D. V. Atkare, *Ferroelectrics*, 2005, **315**, 91–110.
59 W. Zhu and Z. Y. Shen, *J. Mater. Sci.*, 2024, **59**, 2998–3008.
60 X. Qiao, F. Zhang, D. Wu, B. Chen, X. Zhao, Z. Peng, X. Ren, P. Liang, X. Chao and Z. Yang, *Chem. Eng. J.*, 2020, **388**, 124158.
61 R. A. Malik, A. Hussain, A. Maqbool, A. Zaman, C. W. Ahn, J. U. Rahman, T. K. Song, W. J. Kim and M. H. Kim, *J. Am. Ceram. Soc.*, 2015, **98**, 3842–3848.
62 R. A. Malik, A. Hussain, A. Maqbool, A. Zaman, T. K. Song, W. J. Kim and M. H. Kim, *J. Alloys Compd.*, 2016, **682**, 302–310.
63 Q. Zheng, B. Xie, Y. Tian, Q. Wang, H. Luo, Z. Liu and H. Zhang, *J. Materiomics*, 2024, **10**, 845–856.
64 Q. Zheng, B. Xie, Q. Wang, F. Xue, K. Guo, Z. Liu, P. Mao, W. Cao, H. Luo and H. Zhang, *Chem. Eng. J.*, 2024, **483**, 149154.
65 C. Ma, H. Du, J. Liu, L. Kang, X. Du, X. Xi and H. Ran, *Ceram. Int.*, 2021, **47**, 25029–25036.
66 Q. Xua, T. Lia, H. Haoa, S. Zhangb, Z. Wanga, M. Caoa, Z. Yaoa and H. Liua, *J. Eur. Ceram. Soc.*, 2015, **35**, 545–553.
67 Y. Wan, N. Hou, P. Ren, M. Ma, K. Song, F. Yan, X. Lu and G. Zhao, *J. Alloys Compd.*, 2021, **888**, 161591.
68 Z. Li, B. Xie, Z. Liu, K. Guo, K. Li, H. Zhang and H. Luo, *J. Mater. Chem. A*, 2025, **13**, 9339.
69 B. Zheng, Y. Lin, H. Yang, H. Jing, H. Nan, Y. Wang, F. Z. Yao, M. Wang and Q. Yuan, *Adv. Sci.*, 2025, **12**, 2409814.
70 B. Zheng, Q. Yuan, Y. Lin, D. Li, H. Yang, Z. Hong, Y. Ma, Y. Ma, J. Guo and J. Wang, *Adv. Energy Mater.*, 2025, e04126.
71 M. Zhang, H. Yang, Y. Lin, Q. Yuan and H. Du, *Energy Storage Mater.*, 2022, **45**, 861–868.
72 H. Xie, Y. Zhao, J. Xu, L. Yang, C. Zhou, H. Zhang, X. Zhang, W. Qiu and H. Wang, *J. Alloys Compd.*, 2018, **743**, 73–82.
73 P. Jarupoom, P. Jaita, D. R. Sweatman, A. Watcharapasorn and G. Rujijanagul, *Mater. Sci. Eng., B*, 2022, **277**, 115579.
74 H. Luo, H. Liu, H. Huang, Y. Song, M. G. Tucker, Z. Sun, Y. Yao, B. Gao, Y. Ren, M. Tang, H. Qi, S. Deng, S. Zhang and J. Chen, *Sci. Adv.*, 2023, **9**, eade7078.
75 J. Lin, F. Lv, Z. Hong, B. Liu, Y. Wu and Y. Huang, *Adv. Funct. Mater.*, 2024, **34**, 2313879.
76 R. A. Eichel, *Phys. Chem. Chem. Phys.*, 2011, **13**, 368–384.
77 M. Tyunina, *Materials*, 2020, **13**, 5596.
78 L. X. Zhang and X. Ren, *Phys. Rev. B: Condens. Matter Mater. Phys.*, 2005, **71**, 174108.
79 Z. H. Zhao, Y. Dai and F. Huang, *Sustainable Mater. Technol.*, 2019, **17**, e00092.
80 Y. Wang, P. Wang, L. Liu, Y. Wang, Y. Zhao, W. Tian, X. Liu, F. Zhu and J. Shi, *Materials*, 2023, **16**, 4008.
81 F. Ali, W. Raza, X. Li, H. Gul and K. H. Kim, *Nano Energy*, 2019, **57**, 879–902.
82 J. Jacob, N. More, K. Kalia and G. Kapusetti, *Inflammation Regener.*, 2018, **38**, 2.
83 M. A. El-Morsy, N. S. Awwad, H. A. Ibrahium, W. Alharbi, M. Y. Alshahrani and A. A. Menazea, *J. Saudi Chem. Soc.*, 2022, **26**, 101463.
84 M. Safari-Gezaz, M. Parhizkar and E. Asghari, *Sci. Rep.*, 2025, **15**, 149.
85 P. Sriprapha, K. Chokethawai, C. Randorn, N. Chandet, K. Thongkorn, K. Saenkam, W. Boontakam and G. Rujijanagul, *Mater. Today Sustain.*, 2024, **26**, 100710.

86 A. I. Nicoară, V. Cocoș, C. Chircov, R. D. Truşcă and A. Hudiță, *Ceram. Int.*, 2025, **51**, 22327–22339.
87 E. A. Mahdy, K. M. Sahbal, M. Mabrouk, H. H. Beherei and Y. K. Abdel-Monem, *Ceram. Int.*, 2021, **47**, 6251–6261.
88 A. Zerboni, R. Bengalli, G. Baeri, L. Fiandra, T. Catelani and P. Mantecca, *Nanomaterials*, 2019, **9**, 1302.
89 F. Vietanti, Y. J. Lee and Y. J. Chou, *Open Ceram.*, 2025, **22**, 100801.
90 S. Ferraris, S. Yamaguchi, N. Barbani, M. Cazzola, C. Cristallini, M. Miola, E. Vernè and S. Spriano, *Acta Biomater.*, 2020, **102**, 468–480.
91 M. RaeisianAsl, S. Jouybar, S. S. Tafreshi and L. Naji, *Mater. Today Sustain.*, 2025, **29**, 101072.
92 Q. Zhang, J. Chen, J. Feng, Y. Cao, C. Deng and X. Zhang, *Biomaterials*, 2003, **24**, 4741–4748.